Research Square

Preprints are preliminary reports that have not undergone peer review.
They should not be considered conclusive, used to inform clinical practice,
or referenced by the media as validated information.

Defect-mediated carrier transport in tin oxide transparent electrodes via post- annealing atmosphere engineering for silicon heterojunction solar cells

Xuanchu Wang
Ningbo University
Yihuang Su
NingboTech University
Buchao Chen
NingboTech University
Jing Zhang
NingboTech University
Pochuan Yang
Risen Energy Co., LTD
Ying Zhang
Risen Energy Co., LTD
Shiwei Tang
Ningbo University
Weiyan Wang
wangwy@nbt.edu.cn
NingboTech University

Research Article

Keywords: tin oxide transparent electrodes, annealing atmosphere, carrier transport, defects, indium-less silicon heterojunction solar cells

Posted Date: November 16th, 2026

DOI: https://doi.org/10.21203/rs.3.rs-11531678/v1

License: This work is licensed under a Creative Commons Attribution 4.0 International License.
Read Full License

Additional Declarations: No competing interests reported.

Defect-mediated carrier transport in tin oxide transparent electrodes via post-annealing atmosphere engineering for silicon heterojunction solar cells

Xuanchu Wang[1,2], Yihuang Su[2], Buchao Chen[2], Jing Zhang[2], Pochuan Yang[3], Ying Zhang[3], Shiwei Tang[1,*], Weiyan Wang[2,*]

[1]School of Physical Science and Technology, Ningbo University, Ningbo 315211, P. R. China

[2]School of Materials and Energy Engineering, NingboTech University, Ningbo 315100, P. R. China

[3]Risen Energy Co., LTD., Ningbo 315600, P.R. China

[*]Corresponding author:

Shiwei Tang, tangshiwei@nbu.edu.cn;

Weiyan Wang, wangwy@nbt.edu.cn

Abstract

Silicon heterojunction (SHJ) solar cells are promising for high-efficiency terrestrial and low-Earth-orbit photovoltaics owing to their high efficiency, low temperature coefficient, and high bifaciality. However, conventional indium tin oxide transparent electrodes rely on scarce and costly indium, hindering the sustainable development of SHJ technology. In this work, tantalum-doped tin oxide (TTO) was employed as an alternative transparent conductive material, and the effect of post-annealing atmosphere on the optoelectrical properties of TTO films is investigated. After post-annealing at 220 ℃, N_2 and vacuum annealing yields the highest carrier concentration and mobility, respectively. Vacuum annealing improves crystallinity and reduced localized defect states, thereby suppressing carrier scattering and enhancing mobility; whereas N_2 annealing increases the concentration of oxygen-vacancy-related defects, resulting in a higher carrier concentration. The 100 nm TTO film annealed in N_2 achieves a minimum sheet resistance of 244 Ω sq^{-1} and a figure of merit of 2.99 × 10^{-4} $Ω^{-1}$. Indium-less SHJ solar cells are subsequently fabricated using TTO transparent electrodes. Compared with the device based on as-deposited TTO film, this device employing post-annealed TTO film exhibits improved fill factor and power conversion efficiency. These results provide insights into the mechanisms governing the electrical properties of tin oxide-based transparent conductive films and demonstrate the potential of TTO for indium-less SHJ solar cells and other optoelectronic applications.

Keywords: tin oxide transparent electrodes, annealing atmosphere, carrier transport, defects, indium-less silicon heterojunction solar cells

1 Introduction

Silicon heterojunction (SHJ) solar cells, with a power conversion efficiency exceeding 27%, a low temperature coefficient, and a high bifaciality factor,[1-5] are among the most promising technologies for high-efficiency terrestrial and low-Earth-orbit photovoltaic applications.[6,7] However, the conventional indium tin oxide (ITO) transparent electrodes in SHJ solar cells rely on indium. The scarce reserves and high cost of indium pose significant challenges to the large-scale deployment of SHJ photovoltaics.[8-11] As the annual production capacity of photovoltaic modules increases to 3 TW, the indium consumption of solar cells must be substantially reduced from the current 4.23 mg/W to 0.13 mg/W.[12] Therefore, developing SHJ solar cells based on indium-less or indium-free transparent electrodes is of great significance for sustainable development of the photovoltaic technology.

Among the candidate materials for replacing ITO, sputtered tin oxide (SnO_x) films have attracted considerable attention owing to their earth abundance, low cost, and excellent environmental stability.[13-18] Extensive efforts have focused on tailoring their structural and optoelectrical properties through sputtering parameter optimization and elemental doping.[19-25] M. Härtel et al. demonstrated that the optoelectrical properties of SnO_x films strongly depend on the Ar/O_2 ratio, owing to the regulation of carrier concentration by oxygen vacancies, achieving a minimum resistivity of 3.4×10^{-3} Ω·cm.[23] M. Weidner et al. comparatively investigated the properties of Sb- and Ta-doped SnO_x films. Compared with Sb-doped films, the Ta-doped SnO_x (TTO) films exhibited a higher mobility of 25.7 $cm^2 V^{-1} s^{-1}$ and a lower resistivity of 5.4×10^{-4} Ω·cm, which was attributed to improved crystallinity and reduced grain-boundary scattering.[24] H.-K. Kim et al. introduced N during sputtering to promote oxygen vacancy formation, obtaining a sheet resistance of 38.64 Ω sq^{-1} for a 300 nm N-doped SnOx film while maintaining excellent chemical stability.[25] In our previous work, post-annealing at 300 ℃ in H_2 was used to simultaneously increase carrier concentration and mobility, yielding a 150 nm TTO film with a sheet resistance of 91.8 Ω sq^{-1} and an average visible-light transmittance of 79.58%.[26]

Despite these advances, SnO_x films still generally suffer from lower mobility, higher resistivity, and inferior visible-light transmittance compared with ITO, resulting in lower power conversion efficiency (PCE) in SnO_x-based SHJ solar cells.[27,28] Moreover, the relatively high processing temperatures and large film thicknesses commonly employed in previous studies are incompatible with SHJ fabrication. Therefore, simultaneously achieving high mobility, low sheet resistance, and high visible-light transmittance in thin SnO_x films under SHJ-compatible processing conditions remains challenging.

In this work, post-annealing at 220 ℃ was employed to modulate the optoelectrical properties of TTO films. At this relatively low temperature, N_2 and vacuum annealing resulted in the highest carrier concentration and mobility, respectively. The underlying mechanisms were elucidated: N_2 annealing increased the oxygen vacancy concentration, thereby enhancing the carrier concentration, whereas vacuum annealing improved crystallinity and reduced localized defect states, leading to enhanced carrier mobility. As a result, the 100 nm TTO film annealed in N_2 achieved a minimum sheet resistance of 244 Ω sq^{-1} and a high figure of merit of 2.99×10^{-4} Ω^{-1}. Finally, indium-less SHJ solar cells were fabricated with TTO transparent electrodes to establish the correlation between the optoelectrical properties of TTO films and the device performance.

2 Experimental Section

2.1 Thin film and device preparation

Glass substrates were sequentially ultrasonicated in deionized water and isopropanol for 15 min. After cleaning, the substrates were transferred into a radio-frequency magnetron sputtering chamber for the TTO films deposition. TTO films were deposited using a ceramic TTO target containing 1 wt% tantalum (purity 99.99%) with a base pressure of 5×10^{-4} Pa, a O_2/Ar flow ratio of 1.5/80, a sputtering pressure of 0.5 Pa, a sputtering power of 60 W, and substrate temperature of 150 ℃. Under these

deposition conditions, the film growth rate was approximately 10 nm·min^{-1}, and the TTO film thickness was controlled by adjusting the sputtering time. After deposition, the TTO films were post-annealed at 220 ℃ for 10 min under O_2, N_2, or vacuum conditions. During vacuum annealing, the chamber pressure was maintained below 1×10^{-1} Pa. Hereafter, the as-deposited film and the films post-annealed under O_2, N_2, and vacuum were denoted as as-deposited, O_2-PA, N_2-PA, and Vac-PA, respectively. Herein, PA is the abbreviation of post-annealing.

Semi-finished SHJ solar cells with a 100 nm front ITO electrode and a pre-deposited 30 nm rear ITO layer were utilized for device fabrication. The samples were sequentially ultrasonicated in deionized water and isopropanol for 15 min. Then, TTO films were deposited onto rear-side of device using the same magnetron sputtering procedure described above, followed by the post-annealing at 220 ℃ for 10 min. For comparison, 100 nm as-deposited, 100 nm N_2-PA, and 300 nm N_2-PA TTO films were employed as the rear TTO electrodes. Subsequently, 100 nm-thick Ag grid electrodes were deposited on the front and rear sides of the cells by thermal evaporation. The completed solar cell possessed an architecture of Ag/ITO/n-μc-Si:H/i-a-Si:H/n-c-Si/i-a-Si:H/p-a-Si:H/ITO/TTO/Ag, with an effective device area of 4 cm^2.

2.2 Thin film and device characterization

The electrical properties of the TTO films were measured using a Hall measurement system (HL9900, Toho, Japan). The optical properties of the TTO films were characterized using a UV-Vis-NIR spectrophotometer (Lambda 1050+, PerkinElmer, USA). The microstructure and crystalline characteristics of the films were examined by transmission electron microscopy (TEM, JEOL F200, JEOL, Japan), coupled with selected-area electron diffraction (SAED). The surface morphology and roughness of the TTO films were characterized using an atomic force microscope (AFM, Dimension Icon, Bruker, USA) operated in tapping mode. The chemical composition of the films were analyzed by X-ray photoelectron spectroscopy (XPS, K-Alpha, Thermo Scientific, USA) using an Al Kα source (hv =1486.6 eV). Photoluminescence

(PL) spectra were collected using a fluorescence spectrometer (FLS1000, Edinburgh, UK). Electron paramagnetic resonance (EPR) measurements were performed using an EPR spectrometer (EMXplus-6/1, Bruker, Germany). The morphologies of the films and devices were characterized using a scanning electron microscope (SEM, Sigma 300, ZEISS, Germany). The current density-voltage (*J-V*) characteristics of the SHJ solar cells were measured in ambient air using a solar simulator (SS-X50, Enlitech, Taiwan) under AM 1.5G illumination at an intensity of 100 mW cm^{-2}. External quantum efficiency (EQE) spectra were recorded in the wavelength range of 300-1200 nm via an EQE testing system (QE-R3011, Enlitech, Taiwan).

3 Results and Discussion

3.1 Effect of post-Annealing atmosphere on the optoelectrical properties of TTO Films

Post-annealing is an effective method for regulating the properties of sputtered oxide films. Previous studies have shown that, during the annealing of SnO_x films, the modulation of oxygen vacancy and dopant activation may influence carrier density, while the regulation of structural characteristics may affect carrier transport behavior [29]. Preliminary screening of annealing temperature and duration was conducted (Tables S1 and S2). Considering the trade-off between thermal budget and electrical improvement, an annealing temperature of 220 ℃ and a duration of 10 min were selected for subsequent experiments. Figure 1a compares the electrical properties of 100 nm TTO films annealed at 220 ℃ for 10 min under different atmospheres. Compared with the as-deposited film, all post-annealed films exhibited reduced sheet resistance. The sheet resistance decreased from 381 Ω sq^{-1} for the as-deposited film to 330, 244, and 262 Ω sq^{-1} after annealing in O_2, N_2, and vacuum, respectively. Notably, the N_2-annealed film exhibited the lowest sheet resistance, corresponding to a 35.9% reduction. The sheet resistance is given by

$$R_s=\frac{\rho}{t}=\frac{1}{qn\mu t}$$

where R_s, ρ, t, q, n, and μ represent the sheet resistance, electrical resistivity, film thickness, elementary charge, carrier concentration, and Hall mobility, respectively. Since the film thickness remained constant, the reduction in sheet resistance can be attributed primarily to increases in carrier concentration and mobility. As shown in Fig. 1a and Table 1, the carrier concentration increased from 1.414×10^{20} cm^{-3} for the as-deposited film to 1.604×10^{20}, 1.991×10^{20}, and 1.812×10^{20} cm^{-3} after O_2, N_2, and vacuum annealing, respectively. Meanwhile, the Hall mobility increased from 11.6 to 11.8, 12.8, and 13.1 cm^2 V^{-1} s^{-1}, respectively. Thus, both carrier concentration and mobility were enhanced by post-annealing, resulting in reduced sheet resistance. However, their degrees of improvement strongly depended on the annealing atmosphere. O_2 annealing produced the smallest increase in carrier concentration, likely due to the suppression of oxygen vacancy formation. In contrast, N_2 annealing yielded the highest carrier concentration and the lowest sheet resistance, whereas vacuum annealing resulted in the greatest mobility enhancement. These results demonstrate that both thermal treatment and annealing atmosphere play critical roles in determining the electrical properties of TTO films. Thermal treatment can promote dopant activation and structural reconstruction, thereby improving electrical transport.[30] The specific effects of the annealing atmosphere on carrier concentration and mobility are discussed in the following section.

It should be noted that, in our previous work, H_2 annealing at 300 °C resulted in a lower sheet resistance than N_2 annealing. In contrast, previous studies reported that N_2 annealing at relatively low temperatures (200–250 °C) yielded lower sheet resistance,[26] consistent with the present results. These findings suggest that the effect of the annealing atmosphere on the electrical properties of TTO films may depend strongly on the annealing temperature. Although further investigation is required to clarify the underlying mechanism, this is beyond the scope of the present work.

The effect of post-annealing on the optical properties of the films is shown in Fig. 1b, with the corresponding parameters summarized in Table 1. Neither the average transmittance nor absorptance in the wavelength range of 400-1200 nm showed

significant changes after annealing under different atmospheres. This indicates that, although post-annealing substantially improves the electrical properties of the films, it has a limited impact on their optical properties. Notably, the increased carrier concentration did not induce additional near-infrared absorption, preserving the transparency required for TTO electrodes in SHJ solar cells. As shown in Fig. 1c, the optical bandgap of the TTO films remained nearly unchanged after post-annealing under different atmospheres, with values of 3.77–3.78 eV.

To evaluate the overall optoelectrical performance, the Haacke figure of merit (FOM) was calculated over the 400-1200 nm wavelength range, which is relevant to SHJ device operation, according to the following equation:

$$\mathrm{FOM}=\frac{T^{10}}{R_{\mathrm{s}}}$$

where T is the average transmittance over 400-1200 nm and R_s is the sheet resistance. As summarized in Table 1, the FOM increased from $1.79 \times 10^{-4}\ \Omega^{-1}$ for the as-deposited film to 2.10×10^{-4}, 2.99×10^{-4}, and $2.75 \times 10^{-4}\ \Omega^{-1}$ after O_2, N_2, and vacuum annealing, respectively. The N_2-annealed TTO film exhibited the highest FOM, primarily owing to its lowest sheet resistance while maintaining comparable optical properties.

3.2 Mechanism of N_2 and vacuum post-annealing effects on the electrical properties of TTO Films

As shown in Fig. 1a, the samples post-annealed under N_2 and vacuum exhibited the highest carrier concentration and carrier mobility, respectively, indicating that the annealing atmosphere plays a critical role in modulating the electrical properties of the films. Therefore, the mechanisms underlying the enhanced electrical properties induced by N_2 and vacuum annealing, are investigated in detail.

On the one hand, the higher mobility is supposed to be ascribed to the structural and defect characteristics. The HRTEM images in Figs. 2a-c show that all the as-deposited and post-annealed thin films exhibited nanocrystalline features; however, post-annealing significantly altered the degree of lattice ordering and the grain size.

Compared with the as-deposited sample, the lattice fringes became generally clearer and more continuous after annealing in both N_2 and vacuum atmospheres, indicating that annealing promotes atomic rearrangement, structural relaxation, and local crystallographic ordering. Between the two annealing conditions, the N_2-annealed film contained relatively small, densely distributed lattice fringe regions, whereas the vacuum-annealed film exhibited larger continuous lattice fringe regions. The SAED patterns in Figs. 2d-f further distinguish the two annealed films. The N_2-annealed film displays relatively clear and continuous diffraction rings, while the vacuum-annealed film appear more pronounced discrete bright spots along the diffraction rings, in line with the larger continuous lattice-fringe regions observed by HRTEM. The AFM images in Figs. 2g-i revealed that the vacuum post-annealed film exhibits large clustered grains compared with as-deposited and N_2-annealed films. The corresponding three-dimensional AFM images (Fig. S1) further illustrate these topographical differences. The root-mean-square roughness values are 0.409, 0.531, and 0.557 nm, respectively, for the as-deposited, N_2-annealed, and vacuum-annealed samples.

The difference in crystallinity may influence the defects characteristics in films. In the following, the defect state of TTO films is characterized by the Urbach energy. Urbach energy (E_u) values were calculated using the following Equation:

$$\alpha=\alpha_0 exp(\frac{h\nu}{E_u})$$

where α is the absorption coefficient, α_0 is a constant, and $h\nu$ is the photon energy. Normally, the Urbach energy value is considered to represent the width of band-tail states near the absorption edge and the degree of local structural disorder in the band gap of low crystallinity, disordered, or amorphous materials, which is suitable to our case. As shown in Fig. 1c, the Urbach energy decreased from 260 meV for the as-deposited film to 240 meV and 219 meV for the N_2- and vacuum-annealed films, respectively, suggesting a reduction in localized band-tail states and a decrease in local energetic disorder after annealing, particularly under vacuum conditions. The post-annealing thermal treatment facilitates structural relaxation and atomic rearrangement,[31] leading to improved lattice ordering and a narrowed band tail,

thereby reducing the E_u value. Moreover, the annealing atmosphere plays a critical role in regulating oxygen-related defects through oxygen redistribution, which can modify the local coordination environment and promote defect reconfiguration. The enlarged continuous lattice-fringe regions observed in the vacuum-annealed TTO film further confirm the enhanced local structural ordering, contributing to the lowest E_u value among all samples. Consequently, the reduced defect density and improved structural ordering in the vacuum-annealed TTO film suppress carrier trapping and scattering, facilitating carrier transport and resulting in the enhanced Hall mobility shown in Fig. 1a.

On the other hand, to investigate the effect of the annealing atmosphere on the carrier concentration, XPS was employed to characterize the chemical states and composition of the as-deposited, N_2-annealed, and vacuum-annealed TTO films. As shown in Fig. 3a, the O 1s spectra of all films can be deconvoluted into three components corresponding to O–Sn^{4+} (530.7 eV), O–Sn^{2+} (530.5 eV), and adsorbed oxygen/hydroxyl species (532.0 eV). The Sn 3d spectra in Fig. 3b can be similarly deconvoluted into Sn^{4+} and Sn^{2+} components, with the Sn $3d_{5/2}$ and Sn $3d_{3/2}$ peaks located at 486.9 and 495.3 eV for Sn^{4+}, and 486.2 and 494.6 eV for Sn^{2+}, respectively. The peak separation between Sn $3d_{5/2}$ and Sn $3d_{3/2}$ was 8.4 eV, while that between Sn^{4+} and Sn^{2+} was 0.7 eV, consistent with previously reported values.[32] The O/Sn atomic ratio was calculated using the following equation:

$$\mathrm{O/Sn} = \frac{A_O/S_O}{A_{Sn}/S_{Sn}}$$

where A_O represents the fitted peak areas of the O–Sn^{4+} and O–Sn^{2+} components in the O 1s spectrum, excluding adsorbed oxygen/hydroxyl species, and A_{Sn} denotes the corresponding peak areas of the Sn $3d_{5/2}$ and Sn $3d_{3/2}$ components. S_O and S_{Sn} are the relative sensitivity factors of O 1s and Sn 3d, respectively. The O/Sn atomic ratios of the as-deposited, N_2-annealed, and vacuum-annealed films were 1.942, 1.789, and 1.877, respectively, indicating a decrease in the oxygen content after annealing. Notably, the N_2-annealed film exhibited a lower O/Sn ratio than the vacuum-annealed film, suggesting a higher oxygen vacancy concentration under N_2 annealing. This result is

consistent with the higher carrier concentration observed for the N_2-annealed film. It should be noted that Ta was below the detection limit of XPS, owing to its low dopant concentration.

In addition, PL spectroscopy is employed to further evaluate oxygen-vacancy-related defects. As shown in Fig. 3c, all samples exhibited a characteristic emission peak centered at approximately 390 nm, which has been associated with oxygen vacancies.[33] The PL intensity increased after N_2 and vacuum annealing, with the N_2-annealed film exhibiting the strongest emission, further supporting the formation of a higher concentration of oxygen-vacancy-related defects under N_2 annealing. The EPR spectra are shown in Fig. 3d. All samples exhibited a distinct signal at $g \approx 2.002$, confirming the presence of singly charged oxygen-vacancy-related paramagnetic centers. The N_2-annealed film showed the strongest EPR signal, followed by the as-deposited film, whereas the vacuum-annealed film exhibited the weakest signal. These results further indicate that N_2 annealing promotes the formation of EPR-active oxygen-vacancy-related centers. The weakened EPR signal after vacuum annealing may be attributed to the transformation of some oxygen vacancies from EPR-active to EPR-inactive states.

Based on the above results, the N_2-annealed TTO film exhibited the highest concentration of oxygen-vacancy-related defects. This may be attributed to the incorporation of N atoms during N_2 annealing, which is expected to reduce the formation energy of oxygen vacancies and thus promote their formation.[25,34] The resulting increase in oxygen vacancy concentration contributes to the enhanced carrier concentration of the TTO film.

3.3 Effect of film thickness on the optoelectrical properties of TTO films

The optoelectrical characteristics of TTO transparent electrodes directly affect the performance of solar cells. We then compared the optoelectrical properties of TTO films

with different thicknesses using the optimal post-annealing in N_2 atmosphere. Cross-sectional SEM images demonstrated that the thicknesses of the prepared TTO films were increased from ~100 nm to ~400 nm with prolonging sputtering time (Fig. S2). Figure 4a presents the Hall results of the 100-400 nm TTO films with post-annealed in N_2. The sheet resistances of the 100, 200, 300, and 400 nm films were 244, 166, 124, and 94 Ω sq^{-1}, respectively. The mobilities of the 100, 200, 300, and 400 nm films were 12.8, 12.4, 11.8, and 11.4 cm^2 V^{-1} s^{-1}, respectively, showing a slightly decreasing with the increase of films thickness; whereas the corresponding carrier concentrations were 1.991×10^{20}, 1.514×10^{20}, 1.421×10^{20}, and 1.453×10^{20} cm^{-3}, respectively. Considering the limited changes in carrier concentration and mobility, increasing the film thickness effectively improved the sheet resistance of the films. Figure 4b shows the Tauc plots of the TTO films with different thicknesses, together with the corresponding optical bandgaps and Urbach energies. As the film thickness increased from 100 to 400 nm, the optical bandgap decreased slightly from 3.77 to 3.74 eV. The Urbach energies of the 100, 200, 300, and 400 nm films were 240, 260, 285, and 301 meV, respectively. The increase in Urbach energy with film thickness indicates enhanced defect states, which adversely affect carrier transport and result in a corresponding decrease in mobility. This trend is consistent with the dependence of mobility on film thickness obtained from the Hall results.

Increasing the film thickness reduces the sheet resistance but at the same time increases the optical path length within the film, thereby enhancing absorption-, scattering-, and interference-related optical losses. Figure 4c shows the transmittance and absorptance spectra of the TTO films with different thicknesses. The transmittance spectra exhibited pronounced spectral oscillations with increasing thickness, indicating that the film thickness altered the optical path length and interference conditions. Overall, the 100 nm, 200 nm, and 300 nm samples maintained relatively good optical transparency, with average transmittances in the 400-1200 nm wavelength range of 76.96%, 78.80%, and 77.56%, respectively. However, the average transmittance of the 400 nm sample sharply decreased to 74.30%. A further comparison of the average

absorptance showed that, relative to the value of 6.18% for the 100 nm sample, the average absorptance increased slightly to 8.86% and 8.28% for the 200 and 300 nm samples, respectively, and further markedly increased to 12.35% for the 400 nm sample. These results indicate that increasing the film thickness inevitably increase the parasitic absorption within the films, associated with the increased optical path length. While, the degree of parasitic absorption increasement differs among thin films with various thicknesses.

The Haacke figure of merit is further calculated to evaluate the comprehensive optoelectrical of TTO films with different thicknesses. As shown in Table 1, the FOM values of the 100, 200, 300, and 400 nm samples were 2.99×10^{-4} Ω^{-1}, 5.56×10^{-4} Ω^{-1}, 6.36×10^{-4} Ω^{-1} and 5.45×10^{-4} Ω^{-1}, respectively. Among them, the 300 nm TTO film exhibited the highest FOM, indicating that it achieved a relatively favorable balance between reduced sheet resistance and maintained transmittance. Although the 400 nm sample exhibited the lowest sheet resistance, its average transmittance decreased markedly, resulting in a lower FOM value than that of the 300 nm sample. Herein, 300 nm TTO films post-annealed in N_2 is regarded to exhibit the optimal comprehensive optoelectrical properties.

To evaluate the humid-thermal stability of TTO films. Figure 4d shows the changes in sheet resistance of the TTO films with different thicknesses during storage at 85 ℃ and a relative humidity of 85% for 100 h. None of the samples exhibited an abrupt change in sheet resistance during the test. The 100 nm TTO film used for the damp-heat stability test was prepared in a separate deposition batch from that used for the optoelectronic characterization. Its sheet resistance gradually increased from approximately 390 to 465 Ω sq^{-1}, representing the most pronounced change among the tested samples. In contrast, the sheet resistances of the 200 nm, 300 nm, and 400 nm samples remained unchanged throughout the test duration, at approximately 197, 129, and 99 Ω sq^{-1}, respectively. Overall, the relatively small variation in sheet resistance under damp-heat conditions indicates that the TTO films possess good damp-heat stability.

3.4 Performance of SHJ solar cells based on tin oxide transparent electrodes

To establish the correlation between the optoelectrical properties of TTO films and the photovoltaic performance of SHJ solar cells, devices with the architecture Ag/ITO/n-μc-Si:H/i-a-Si:H/n-c-Si/i-a-Si:H/p-a-Si:H/ITO/TTO/Ag were fabricated, as schematically displayed in Fig. 5a. Herein, The rear ITO transparent conductive layer was partially replaced with TTO films, including as-deposited 100 nm TTO, 100 nm TTO post-annealed in N_2, and 300 nm TTO post-annealed in N_2.

Figure 5b presents the *J-V* curves of the SHJ solar cells with different rear TTO electrodes, and corresponding photovoltaic parameters are shown in Table 2. The device employing a 100 nm as-deposited TTO electrode exhibited a V_{oc}, J_{sc}, FF and PCE of 0.712 V, 39.80 mA cm^{-2}, 78.1%, and 22.15%, respectively. The device employing a 100 nm N_2-annealed TTO electrode demonstrated an increased PCE of 22.82%, with corresponding V_{oc}, J_{sc}, and FF of 0.713 V, 38.80 mA cm^{-2}, and 82.5%, respectively. The device based on the 300 nm N_2-annealed TTO electrode exhibited a V_{oc}, J_{sc}, FF, and PCE of 0.710 V, 37.99 mA cm^{-2}, 83.9%, and 22.63%, respectively. Herein, the current density values of these devices were obtained from the EQE measurements shown in Fig. 5c. It was found that the FF and J_{sc} value of devices varied for different TTO films. Among the three devices, the one with the 100 nm N_2-annealed TTO electrode achieved the highest PCE, corresponding to a relative improvement of 3.0% compared with the device using the 100 nm as-deposited TTO electrode.

Compared with the device employing the as-deposited TTO film, the devices employing post-annealed TTO films as transparent electrodes exhibited increased FF values. The device based on the 300 nm post-annealed TTO film showed the highest FF. The increased FF is mainly attributed to the decreased sheet resistance of TTO film by post-annealing. Apart from FF, obvious variation is also observed in J_{sc}. The J_{sc} values of the devices using 100 nm as-deposited TTO, 100 nm post-annealed TTO, and 300 nm post-annealed TTO electrodes decreased in turn. This decrease can be attributed

to two factors. First, parasitic absorption in the TCO layers increased with increasing TTO thickness. The average absorptance over 400-1200 nm was 6.59%, 6.18%, and 8.28% for the 100 nm as-deposited TTO, 100 nm N_2-annealed TTO, and 300 nm N_2-annealed TTO films, respectively. The higher absorptance of the 300 nm TTO film therefore results in greater parasitic optical loss. Second, the variation in J_{sc} is also associated with differences in the refractive index of the TTO films, which affect the rear-side optical reflection. As shown in Fig. S3, the refractive index of TTO was higher than that of ITO over the visible–near-infrared wavelength range. After N_2 annealing, the refractive index of TTO decreased and became closer to that of ITO. According to the Fresnel equation:

$$R_{12}=\left|\frac{n_1-n_2}{n_1+n_2}\right|^2$$

where R_{12} represents the reflectance at the interface between materials with refractive indices n_1 and n_2. The interfacial reflectance depends on the refractive-index contrast between the adjacent layers, with a smaller difference generally resulting in lower reflection. Therefore, compared with the ITO/as-deposited TTO interface, the ITO/N_2-annealed TTO interface exhibits reduced interfacial reflection. Since the TTO layer is located on the rear side of the SHJ solar cell, long-wavelength photons transmitted through the silicon absorber can be reflected back into the wafer for a second absorption. The reduced reflection at the ITO/TTO interface may therefore decrease the photon flux returning to the silicon wafer, contributing to the reduction in J_{sc}.

4 Conclusions

In this work, the effects of post-annealing atmosphere and film thickness on the optoelectrical properties of TTO films were systematically investigated. At a post-annealing temperature of 220 ℃, N_2 and vacuum annealing yielded the highest carrier concentration and mobility, respectively. N_2 annealing increased the concentration of oxygen-vacancy-related defects, thereby enhancing the carrier concentration, whereas vacuum annealing improved crystallinity and reduced defect states, leading to reduced

carrier scattering and enhanced mobility. Consequently, the 100 nm N_2-annealed TTO film achieved a minimum sheet resistance of 244 Ω sq^{-1} and a high figure of merit of 2.99×10^{-4} Ω^{-1}. Moreover, increasing the TTO thickness from 100 to 300 nm further improved the overall optoelectrical properties of the films. Indium-less SHJ solar cells were subsequently fabricated using TTO transparent electrodes. The device incorporating post-annealed TTO exhibited improved FF and PCE compared with the device employing as-deposited TTO, demonstrating the strong correlation between the optoelectrical properties of TTO electrodes and the photovoltaic performance of SHJ solar cells.

Acknowledgement

This work was supported by the National Key Research and Development Plan Project (No. 2024YFB3813904), Ningbo Key Research and Development Project (No. 2024Z243), and Ningbo Science and Technology Project (No. 2022-DST-004).

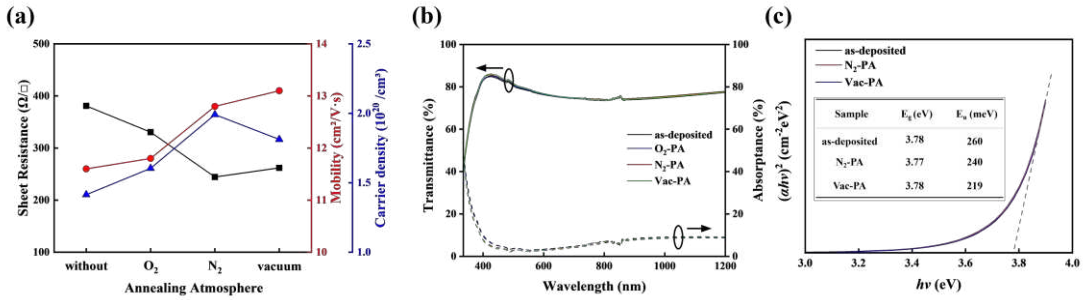


Fig. 1 Effect of post-annealing atmosphere on the electrical and optical properties of TTO films. (a) Sheet resistance, carrier mobility, and carrier concentration; (b) transmittance and absorptance spectra; (c) Tauc plots with the corresponding optical bandgaps and Urbach energies of the as-deposited, N_2-annealed, and vacuum-annealed TTO films.

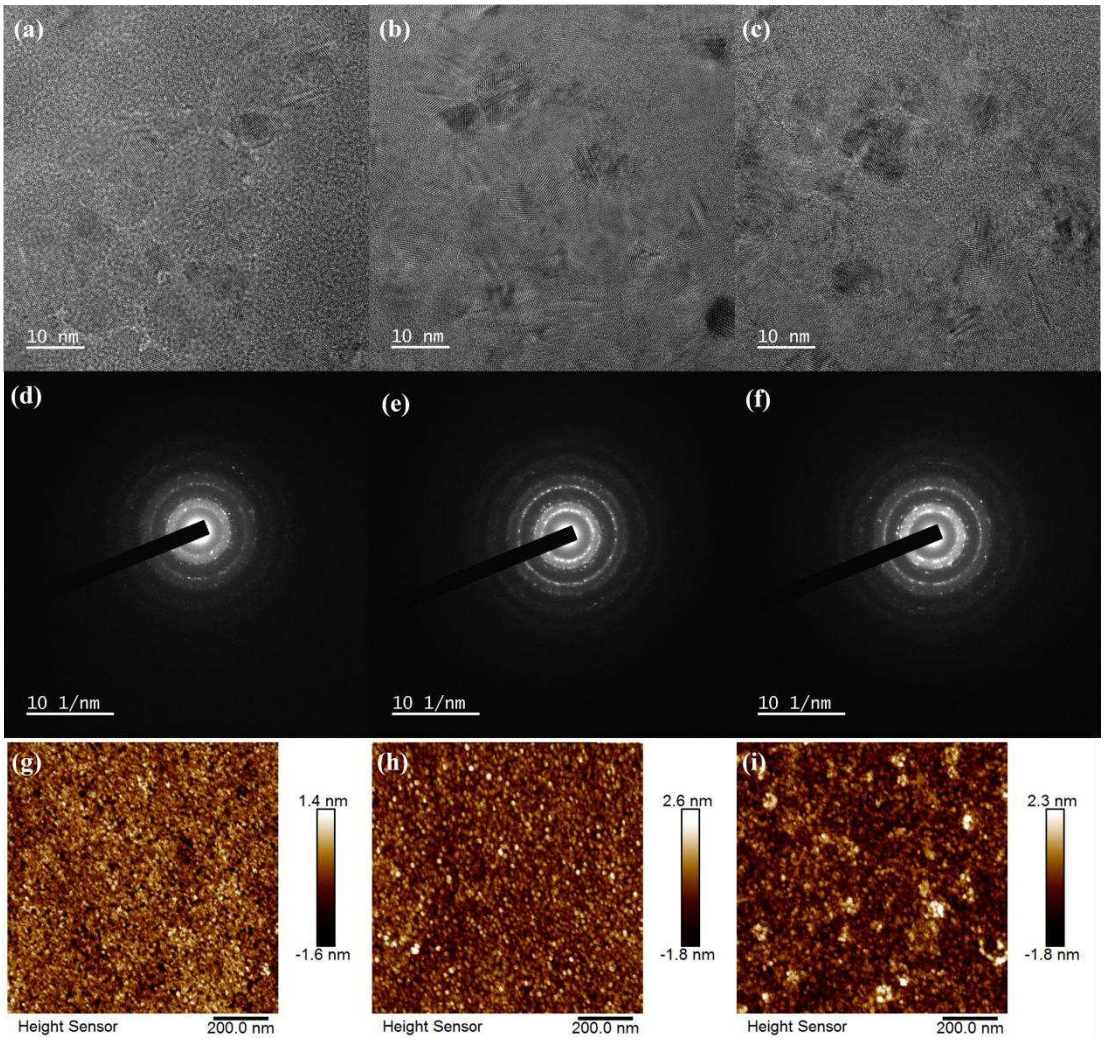


Fig. 2 Microstructure and surface morphology of TTO films. (a–c) HRTEM images, and (d–f) SAED patterns; (g–i) AFM morphology images. In each row, the images from left to right correspond to the as-deposited, N_2-PA, Vac-PA samples.

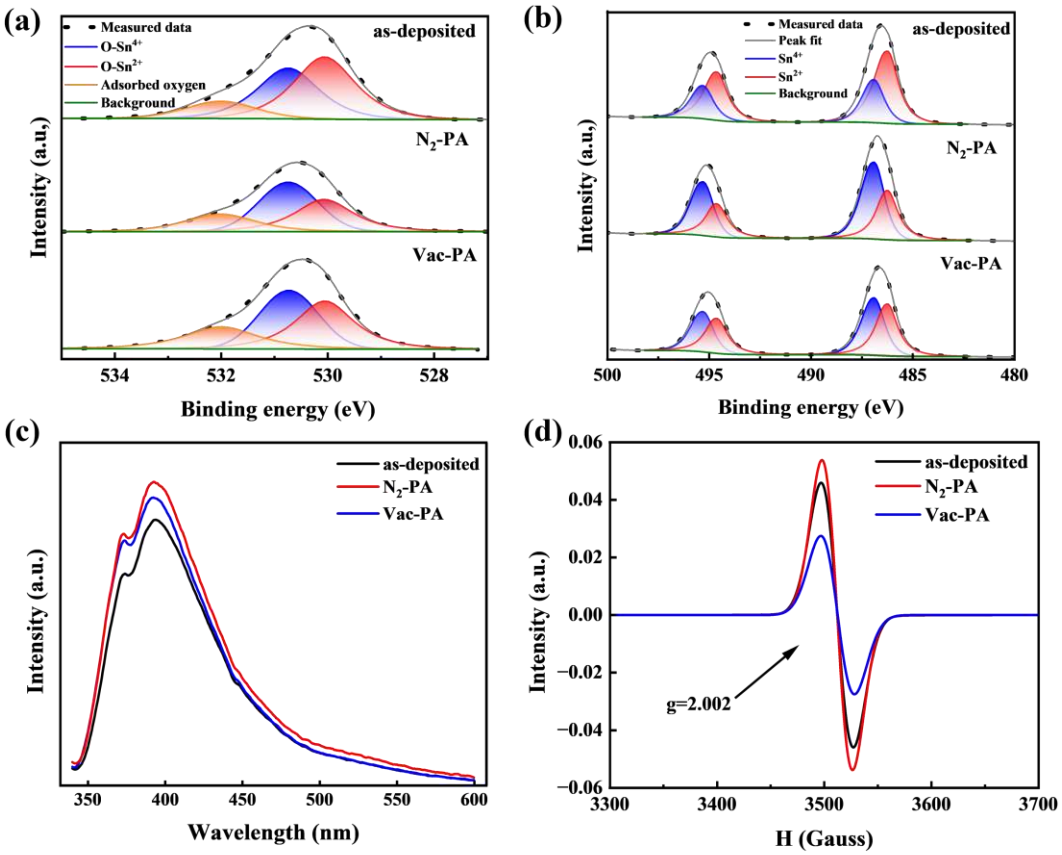


Fig. 3 (a) O 1s XPS; (b) Sn 3d XPS; (c) PL; (d) EPR of the as-deposited, N_2-PA, and Vac-PA TTO films.

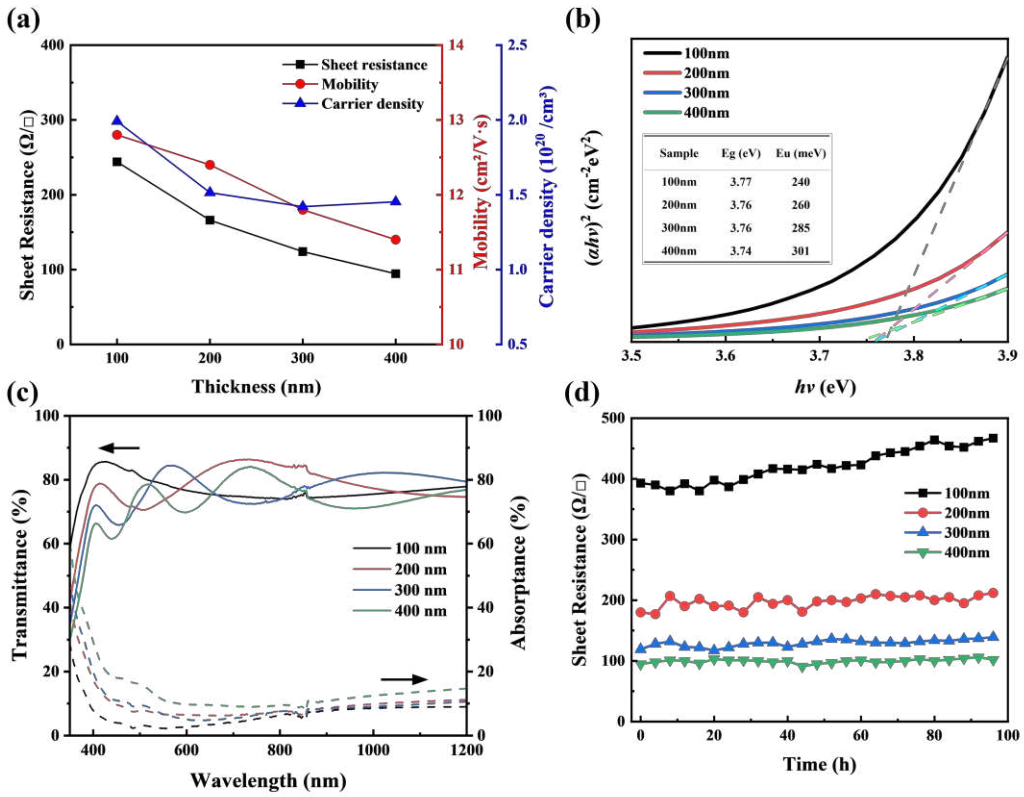


Fig. 4 Electrical, optical, and stability characteristics of N_2-PA TTO films with different thicknesses. (a) Sheet resistance, mobility, and carrier concentration; (b) Tauc analysis with the extracted optical bandgaps and Urbach energies; (c) transmittance and absorptance spectra; and (d) sheet resistance during damp-heat testing at 85 ℃ and 85% RH.

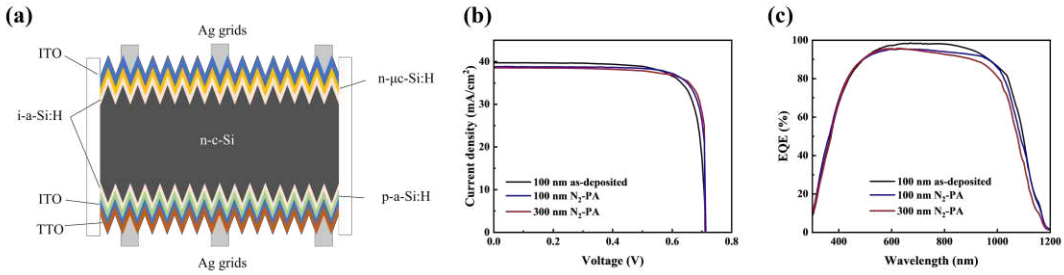


Fig. 5 Photovoltaic performance of SHJ solar cells with TTO rear electrodes. (a) Schematic of the SHJ solar cell structure incorporating a TTO layer; (b) *J-V* characteristics of devices with 100 nm as-deposited, 100 nm N_2-PA, and 300 nm N_2-PA TTO electrodes; and (c) corresponding EQE spectra.

Table 1 Summary of the optoelectrical properties of TTO films with different film thicknesses post-annealed under various atmospheres.

Thickness (nm)	Post-annealing atmosphere	Sheet resistance (Ω sq^{-1})	Average transmittance (%) (400-1200 nm)	FOM ($10^{-4}\cdot\Omega^{-1}$)
100	as-deposited	381	76.43	1.79
100	O_2	330	76.56	2.10
100	N_2	244	76.96	2.99
100	Vac	262	76.85	2.75
200	N_2	166	78.80	5.56
300	N_2	124	77.56	6.36
400	N_2	94	74.30	5.45

Table 2 Photovoltaic parameters of SHJ solar cells incorporating 100 nm as-deposited, 100 nm N_2-annealed, and 300 nm N_2-annealed TTO rear electrodes.

Sample	V_{oc} (V)	J_{sc} (mA/cm^2)	FF (%)	PCE (%)
100 nm as-deposited	0.712	39.80	78.1	22.15
100 nm N_2-PA	0.713	38.80	82.5	22.82
300 nm N_2-PA	0.710	37.99	83.9	22.63

References:

[1] Xie Z, Lu H, Yang G, et al. 27%-efficiency silicon heterojunction cell with 98.6% cell-to-module ratio driving new momentum towards the 29.4% limit[J]. Nature Communications, 2025, 16(1): 9421.

[2] Wang G, Su Q, Tang H, et al. 27.09%-efficiency silicon heterojunction back contact solar cell and going beyond[J]. Nature Communications, 2024, 15(1): 8931.

[3] Nan C, Hao Y, Huang X, et al. Investigation on temperature dependence of recent high-efficiency silicon solar modules[J]. Solar Energy Materials and Solar Cells, 2024, 266: 112649.

[4] Ru X, Qu M, Wang J, et al. 25.11% efficiency silicon heterojunction solar cell with low deposition rate intrinsic amorphous silicon buffer layers[J]. Solar Energy Materials and Solar Cells, 2020, 215: 110643.

[5] Han C, Santbergen R, van Duffelen M, et al. Towards bifacial silicon heterojunction solar cells with reduced TCO use[J]. Progress in Photovoltaics: Research and Applications, 2022, 30(7): 750-762.

[6] Cariou R, Danel A, Enjalbert N, et al. Investigation of p-type silicon heterojunction radiation hardness[J]. IEEE Journal of Photovoltaics, 2023, 14(1): 41-45.

[7] Le A H T, Augusto A, Sai H, et al. Silicon's cosmic comeback: Temperature-dependent performance and radiation stability of ultra-thin silicon heterojunction solar cells for space applications[J]. Materials Today Energy, 2026, 57: 102245.

[8] Werner T T, Mudd G M, Jowitt S M. The world's by-product and critical metal resources part III: A global assessment of indium[J]. Ore Geology Reviews, 2017, 86: 939-956.

[9] Song H L, Wang C, Sun K, et al. Material efficiency strategies across the industrial chain to secure indium availability for global carbon neutrality[J]. Resources Policy, 2023, 85(B): 103895.

[10] Razzaq A, Allen T G, Liu W, et al. Silicon heterojunction solar cells: Techno-economic assessment and opportunities[J]. Joule, 2022, 6(3): 514-542.

[11] Dong G, Li J, Zhao Y, et al. Highly efficient silicon heterojunction solar cells with ZnO:Al transparent electrode and transition metal doped indium oxide interfacial layer[J]. Progress in Photovoltaics: Research and Applications, 2023, 31(9): 931-938.

[12] Zhang Y, Kim M, Wang L, et al. Design considerations for multi-terawatt scale manufacturing of existing and future photovoltaic technologies: challenges and opportunities related to silver, indium and bismuth consumption[J]. Energy & Environmental Science, 2021, 14(11): 5587-5610.

[13] Aragón F H, Aquino J C R, Gomes N C S, et al. Characterization of polycrystalline SnO_2 films deposited by DC sputtering technique with potential for technological applications[J]. Journal of the European Ceramic Society, 2017, 37(10): 3375-3380.

[14] Moure-Flores F D, Quiñones-Galván J G, Hernández-Hernández A, et al. Structural, optical and electrical properties of Cd-doped SnO_2 thin films grown by RF reactive magnetron co-sputtering[J]. Applied Surface Science, 2012, 258(7): 2459-2463.

[15] Belayachi W, Ferblantier G, Fix T, et al. SnO_2 films elaborated by radio frequency magnetron sputtering as potential transparent conducting oxides alternative for organic solar cells[J]. ACS Applied Energy Materials, 2022, 5(1): 170-177.

[16] Xu B, Ren X G, Gu G R, et al. Structural and optical properties of Zn-doped SnO_2 films prepared by DC and RF magnetron co-sputtering[J]. Superlattices and Microstructures, 2016, 89: 34-42.

[17] Ferreira M, Loureiro J, Nogueira A, et al. SnO_2 thin film oxides produced by rf sputtering for transparent thermoelectric devices[J]. Materials Today: Proceedings, 2015, 2(2): 647-653.

[18] Wang Y H, Ma J, Ji F, et al. Structural and photoluminescence characters of SnO_2:Sb films deposited

by RF magnetron sputtering[J]. Journal of Luminescence, 2005, 114: 71-76.
[19] Yu C, Zou Q, Wang Q, et al. Silicon solar cell with undoped tin oxide transparent electrode[J]. Nature Energy, 2023, 8(10): 1119-1125.
[20] Tao Y, Zhu B, Yang Y, et al. The structural, electrical, and optical properties of SnO_2 films prepared by reactive magnetron sputtering: Influence of substrate temperature and O_2 flow rate[J]. Materials Chemistry and Physics, 2020, 250: 123129.
[21] Zhu B L, Zhao X, Hu W C, et al. Structural, electrical, and optical properties of F-doped SnO or SnO_2 films prepared by RF reactive magnetron sputtering at different substrate temperatures and O_2 fluxes[J]. Journal of Alloys and Compounds, 2017, 719: 429-437.
[22] Al-Kuhaili M F. Co-sputtered tantalum-doped tin oxide thin films for transparent conducting applications[J]. Materials Chemistry and Physics, 2021, 257: 123749.
[23] Härtel M, Harter A, Erfurt D, et al. Low resistivity sputter deposited SnO_x thin films: an indium-free transparent conductive cxide?[J]. physica status solidi (RRL)-Rapid Research Letters, 2025, 19(11): 2400404.
[24] Weidner M, Jia J, Shigesato Y, et al. Comparative study of sputter-deposited SnO_2 films doped with antimony or tantalum[J]. Physica Status solidi (b), 2016, 253(5): 923-928.
[25] Seok H J, Kim S H, Yeom K M, et al. Cost-effective transparent N-doped tin oxide electrodes with excellent thermal and chemical stabilities enabling stable perovskite photovoltaics based on tin oxide electron transport layer[J]. Advanced Energy Materials, 2024, 14(13): 2303859.
[26] Chen B, Yao L, Li C, et al. Tantalum-doped tin oxide films with post-annealing in H_2 strategy enabling improved performance of indium-free perovskite solar cells[J]. Small, 2025, 21(46): e08172.
[27] Koida T, Matsui T, Sai H. Indium-free silicon heterojunction solar cells: achieving high conductivity with magnetron-sputtered SnO_2[J]. Progress in Photovoltaics: Research and Applications, 2026, 1-12.
[28] Zhong G, Meng H, Wu X, et al. Properties and application of Ta-doped SnO_2 and ITO stacked films for SHJ solar cells[J]. Solar Energy, 2025, 301: 113907.
[29] Zou Q, Yu C, Zhao Y, et al. Tantalum doped tin oxide enabled indium-free silicon heterojunction solar cells with efficiency over 25%[J]. Nano Energy, 2024, 131: 110206.
[30] Jung J S, Park S J, Ye J H, et al. Optical, structural, and electrical properties of sputter-deposited SnOx thin films[J]. Thin Solid Films, 2022, 747: 139139.
[31] Amato A, Terreni S, Granata M, et al. Observation of a correlation between internal friction and urbach energy in amorphous oxides thin films[J]. Scientific Reports, 2020, 10(1): 1670.
[32] Xue J, Liu K, Liu B, et al. UV-blue photodetectors based on n-SnOx/p-diamond heterojunctions[J]. Materials Letters, 2019, 257: 126621.
[33] Ghosh S, Khan G G, Mandal K. Defect-driven magnetism in luminescent n/p-type pristine and Gd-substituted SnO_2 nanocrystalline thin films[J]. ACS Applied Materials & Interfaces, 2012, 4(4): 2048-2056.
[34] Livraghi S, Barbero N, Agnoli S, et al. A multi-technique comparison of the electronic properties of pristine and nitrogen-doped polycrystalline SnO_2[J]. Physical Chemistry Chemical Physics, 2016, 18(32): 22617-22627.

Supplementary Files

This is a list of supplementary files associated with this preprint. Click to download.

- supportinginformation.docx